Mon. Not. R. Astron. Soc. **000**, 000–000 (0000) Printed 15 August 2008 (MN LATEX style file v2.2)

Quantifying mass-loss rate and wind porosity using the X-ray emission line profiles of ζ Puppis

David H. Cohen,[1⋆] Maurice A. Leutenegger,[2] Emma E. Wollman,[1]
Stanley P. Owocki,[3] Richard H. D. Townsend[3,4], Janos Zsargó[5], D. John Hillier[5]
[1] *Swarthmore College, Department of Physics and Astronomy, Swarthmore, Pennsylvania 19081, USA*
[2] *NASA/Goddard Space Flight Center, Laboratory for High Energy Astrophysics, Code 622, Greenbelt, Maryland 20771, USA*
[3] *University of Delaware, Bartol Research Institute, Newark, Delaware 19716, USA*
[4] *University of Wisconsin, Department of Astronomy, Madison, 475 N. Charter St., Madison, Wisconsin 53706, USA*
[5] *University of Pittsburgh, Department of Physics and Astronomy, 3941 O'Hara St., Pittsburgh, Pennsylvania 15260, USA*

15 August 2008

ABSTRACT

We fit X-ray line profile models, including the effects of large-scale wind porosity, to the high-resolution *Chandra* spectrum of the O4 supergiant ζ Pup. We probe the importance of porosity in two specific ways: by comparing the fit quality of porous and non-porous models for individual line profiles, and also by studying the trend in profile shape for many profiles as a function of wavelength. Individual lines can be fit by both non-porous models and porous models that assume spherical clumps, although for the higher signal-to-noise lines, the non-porous models are always preferred. As the mass-loss rate and the porosity length are nearly degenerate parameters, we explore the trade-offs between the parameters and find that the porosity lengths required to accommodate the traditional mass-loss rate of ζ Pup, 8×10^{-6} $M_\odot$ yr^{-1}, are very high, with $h_\infty > R_*$. Porous models that assume oblate, or flattened, clumps, produce profiles with a different overall shape, and one that does not provide good fits to the data. We also find that there is in fact a significant trend in optical depth as a function of wavelength over the range 6 to 22 Å. This trend is consistent with the expected atomic opacity, but is inconsistent with a highly porous medium, in which the optical depth is governed by the geometrical cross-section of the clumps. From the fits to these lines under the assumption that porosity does not affect the opacity, we derive a mass-loss rate of 3.0×10^{-6} $M_\odot$ yr^{-1}, which represents a factor of ~ 3 reduction of the traditional mass-loss rate derived assuming no wind clumping, and is consistent with more recent determinations that include small-scale clumping. *Note to coauthors: I wonder if we should add a sentence about the CNO abundances and how the sub-solar net abundances make the mass-loss rate determination about a factor of two higher than we'd find if we assumed a solar C + N + O.*

Key words: stars: early-type – stars: mass-loss – stars: winds, outflows – stars: individual: ζ Pup – X-rays: stars

1 INTRODUCTION

The dense and highly supersonic radiation-driven winds of O stars are generally supposed to be the site of X-ray production in these massive stars. Broadened X-ray emission line profiles ($v_{\rm hwhm} \approx 1000$ km s^{-1}), first measured with *XMM-Newton* and *Chandra* early in this decade, provide direct evidence for hot plasma kinematics consistent with the same beta velocity law that describes the bulk of the cool ($T < T_{\rm eff}$) wind (Kahn et al. 2001; Cassinelli et al. 2001; Kramer et al. 2003). This hot, X-ray emitting plasma is thought to be produced by shock heating of a small fraction of the wind to temperatures of a few million K, and it is generally supposed that the line-driven instability (LDI) is the cause of the shocks (Lucy & White 1980; Owocki et al. 1988; Feldmeier et al. 1997; Dessart & Owocki 2003). The high-resolution X-ray spectra not only provide information about the hot, X-ray emitting wind component, they also provide important information about the bulk, cool wind component which attenuates the emitted X-rays.

⋆ E-mail: cohen@astro.swarthmore.edu

The early O supergiants, with the highest mass-loss rates, are expected to have winds that are quite optically thick to X-rays (Hillier et al. 1993). One readily observable effect of optically thick winds is the apparent blue shift and asymmetry of emission lines, which arises because red shifted X-rays emitted from the back of the wind are preferentially absorbed compared to blue shifted photons from the front hemisphere of the wind (MacFarlane et al. 1991; Ignace 2001; Owocki & Cohen 2001). The degree of blue shift and asymmetry is governed by a single parameter that describes the fiducial optical depth, $\tau_* \equiv \frac{\dot{M}\kappa}{4\pi R_* v_\infty}$. So, the line profile shape, through τ_*, provides a powerful diagnostic of the mass-loss rate.

This X-ray line profile mass-loss rate diagnostic is independent of the small-scale clumping (microclumping) that affects density-squared diagnostics of mass loss, like Hα and radio free-free emission. Evidence has recently emerged that microclumping does affect these traditional mass-loss rate diagnostics, and the mass-loss rates of OB stars are starting to be revised downward (Bouret et al. 2005; Fullerton et al. 2006; Puls et al. 2006). X-ray line profiles can provide an independent measurement of mass-loss rate that is not sensitive to microclumping or dependent on detailed knowledge of the ionization state of subdominant ion stages in the wind. The initial quantitative analysis of resolved X-ray profiles, which are less blue shifted and asymmetric than expected, indicated that lower mass-loss rates are favored (Kramer et al. 2003; Cohen et al. 2006). One goal of this paper is, for the first time, to make a quantitative determination of an O star's mass-loss rate from the analysis of its X-ray line profiles.

It has been shown, though, that large-scale clumping – so-called macroclumping – can reduce the effective opacity of the wind and could, in principle, account for the only modestly shifted and asymmetric X-ray profiles that are observed in many O stars (Feldmeier et al. 2003; Oskinova et al. 2004, 2006; Owocki & Cohen 2006). This effect only occurs once individual clumps become optically thick in the X-ray continuum, so that opacity can be effectively hidden in the interior of clumps. When this criterion is met, we say that the wind is porous. Photon escape from the wind is enhanced by this porosity and the wind's effective opacity is reduced. The key parameter that describes the effects of porosity on X-ray line profiles is the porosity length, $h \equiv \ell/f = L^3/\ell^2$ (Owocki & Cohen 2006), where ℓ is the characteristic clump size scale, L is the characteristic interclump spacing, and f is the volume filling factor of clumps (the interclump medium is assumed to contain negligible mass). In the limit of completely optically thick, geometrically thin clumps ("shell fragments" in the parlance of Feldmeier et al. (2003), which are analogous to the oblate clump model of porosity that we employ in this paper), the porosity length is also the photon mean free path in the radial direction, or the radial interclump spacing.

Another goal of this paper, then, is to quantitatively assess the evidence for wind porosity in the observed X-ray line profiles. We do this in two different ways: (1) we fit models of line profiles that include both the mass-loss rate (via τ_*) and the porosity (via h_∞, the porosity length in the far wind) and jointly constrain the values of these model parameters; and (2) we fit line-profile models without porosity to the many lines in the spectrum and assess the evidence for a trend in τ_* with wavelength. In the case of porosity-dominated effective wind opacity (optically thick macroclumping), the cross section to X-rays is governed by the geometric cross section of the clumps, which is wavelength independent, and therefore no trend is expected. In the case where porosity is negligible, the wind opacity is controlled by atomic cross sections (due to photoelectric absorption) of abundant heavy elements in the wind, which is wavelength dependent. We note, though, that the wavelength dependence of the wind opacity is complicated and dependent on the abundances in the wind and on the ionization balance, and therefore we include detailed modeling of the wind ionization and opacity in this paper.

Even in the case that the effects of porosity and atomic opacity cannot be definitively disentangled, we can still quantitatively explore the trade-offs between them. Specifically, in this paper, we assess for the first time just how much porosity (what values of h_∞) are required to fit the data with the traditional, higher mass-loss rates. After making these determinations for the strong lines in the *Chandra* spectrum of ζ Pup, we assess the realism of the derived porosity lengths in light of the small-scale wind structure generated in state-of-the-art two-dimensional radiation hydrodynamics simulations of the LDI in O star winds (Dessart & Owocki 2003).

Finally, it has been suggested that oblate (flattened) clumps, with their surfaces oriented parallel to the star's surface, are especially good at producing symmetric and unshifted line profiles (Oskinova et al. 2006). We therefore include this effect in our line-profile model and fit these models to the data to quantitatively assess whether oblate clumps can in fact account for the observed profile shapes.

The paper is organized as follows: We begin by describing the *Chandra* data set and defining a sample of well behaved emission lines for our analysis in §2. We also briefly evaluate the stellar and wind properties of ζ Pup in this section. In §3 we describe the empirical line profile model for X-ray emission lines, with and without porosity. We also introduce our oblate clump porosity line profile model in this section (*Note to coauthors: Or we reference it, if it will appear in a separate paper.*). And we show how porosity affects X-ray emission line profiles, including how its effects on the profile morphologies differ from those caused by reduced mass-loss rates. In §4 we describe our procedure for analyzing data with the line-profile models presented in the previous section. In §5 we present our results, and in §6 we discuss their implications, including a consideration of wavelength-dependent wind opacity and the results of simulations of wind structure induced by the line-driven instability. In §7 we conclude that the line profile shapes in the *Chandra* grating spectrum of ζ Pup require a mass-loss rate of 3.0×10^{-6} $M_\odot$ yr^{-1}, and that higher mass-loss rates can be accommodated if the effective optical depth of the wind is reduced by porosity, but that unrealistically large values of the porosity length are required for consistency with the literature mass-loss rates. We also conclude that the wavelength dependence of the profile properties is consistent with mass-loss rate reduction and not with the gray effective opacity implied by significant porosity effects. And, finally, we conclude that line-profile models with flattened clumps do not provide good fits to the data.

2 THE *Chandra* GRATING SPECTRUM OF ζ Pup

2.1 The data

All the data we use in this paper was taken on 28-29 March 2000 in a single, 68 ks observation using the *Chandra* High-Energy Transmission Grating Spectrometer (HETGS) in conjunction with the Advanced CCD Imaging Spectrometer (ACIS) detector in spectroscopy mode. This is a photon counting instrument with an extremely low background and high spatial resolution ($\approx 1''$). The first-order grating spectra we analyze have a total of 21,684 counts, the vast majority of which are in emission lines, as can be seen in Fig. 1. We modeled every line in the two spectra, as we describe in §4 and §5, and indicate in this figure which of the lines we deemed to be reliable. We only include lines in our analysis that are not so weak or severely blended that interesting parameters of the line-profile models cannot be reliably constrained.

The HETGS assembly has two grating arrays - the Medium Energy Grating (MEG) and the High Energy Grating (HEG) - with spectral resolutions of 0.0023 Å and 0.0012 Å, respectively. This corresponds to a resolving power of $\mathcal{R} \approx 1000$, or a velocity of 300 km s^{-1}, at the longer wavelength end of each grating. The wind-broadened X-ray lines of ζ Pup are observed to have $v_{\rm fwhm} \approx 2000$ km s^{-1}, and so are very well resolved by *Chandra*. The wavelength calibration of the HETGS is accurate to 50 km s^{-1} (Marshall et al. 2004).

The two gratings, detector, and telescope assembly have significant response from roughly 2 Å to 30 Å, with typical effective areas of tens of cm^2, and a strong function of wavelength. In practice, the shortest wavelength line with significant flux in the relatively soft X-ray spectra of O stars like ζ Pup is the Si XIV Lyman-alpha line at 6.182 Å, and the longest wavelength line is the N VII Lyman-alpha line at 24.781 Å. The HEG response is negligible for lines with wavelengths longer than about 16 Å.

The X-ray spectrum of ζ Pup consists primarily of emission lines from H-like and He-like ionization stages of N, O, Ne, Mg, and Si, and numerous L-shell lines of iron, primarily Fe XVII. The Lyα lines and often the β and even γ lines of the Lyman series are seen for the H-like ions. There is a weak bremsstrahlung continuum beneath these lines. Overall, the spectrum is consistent with an optically thin, thermal plasma in ionization equilibrium with a range of temperatures from one to several million degrees present. It is possible that there are deviations from equilibrium, although the spectrum is not of high enough quality to show this. There is some evidence from the *XMM-Newton* RGS spectrum that a few of the emission lines are optically thick (Leutenegger et al. 2007); a possibility we will take into account when modeling those lines (*Note to coauthors: we have not yet modeled these lines with a profile model that explicitly includes resonance scattering; we'll do it soon. Note that neglect of resonance scattering will lead to an underestimate of* τ_*.).

2.2 The star

ζ Puppis is nearby ($d = 335^{+12}_{-11}$ pc)[1], single, runaway early O supergiant that shows the enhanced nitrogen and deficient carbon and oxygen that is indicative of CNO cycle processed material. Helium is also overabundant. The star's rapid rotation may explain the photospheric abundance anomalies, though it has also been claimed that it had a close binary companion that exploded as a supernova, rendering ζ Pup a runaway and perhaps explaining its anomalous abundances (Vanbeveren et al. 1998). Detailed spectral synthesis has been carried out from the UV to the IR to determine the stellar and wind properties of ζ Pup, which we list in Table 1. Most of these are taken from Puls et al. (2006). There is a range of wind property determinations in the extensive literature on ζ Pup. The terminal velocity of the wind may be as low as 2200 km s^{-1} (Lamers & Leitherer 1993), and as high as 2485 km s^{-1} (Prinja et al. 1990). Mass-loss rate determinations vary as well, partly because of the uncertainty in the distance, but also because each mass-loss rate diagnostic is subject to uncertainty: density squared diagnostics like Hα and free-free emission are affected by clumping, no matter the size scale and optical depth of the clumps. Mass-loss rates from UV absorption lines are subject to uncertain ionization corrections. In the last few years, microclumping has started to be taken into account when deriving mass-loss rates from both density-squared diagnostics and UV absorption diagnostics. We list several mass-loss rate determinations in the table, with notes about the assumptions behind each determination. The X-ray line profile diagnostics of mass-loss rate that we employ in this paper are not directly affected by microclumping; only by macroclumping and the associated porosity.

The star shows periodic variability in various UV wind lines as well as Hα (Berghoefer et al. 1996). Its broadband X-ray properties are normal for an O star, with $L_{\rm x} \approx 10^{-7} L_{\rm Bol}$ and a soft spectrum (Hillier et al. 1993), dominated by optically thin thermal line and free-free emission from plasma with a temperature of a few million degrees. The emission measure filling factor of the wind is small, roughly one part in 10^3. Weak soft X-ray variability, with an amplitude of 6 percent, and a period consistent with the 18 hr H$_\alpha$ period, was detected with *ROSAT* (Berghoefer et al. 1996). This low-level variability appears not to affect the *Chandra* data.

[1] The original Hipparcos distance determination (Perryman et al. 1997) had rather large error bars (429^{+120}_{-77} pc); while the value we quote in the table is from a recent reanalysis of the data (van Leeuwen 2007a,b). The derived stellar parameters and mass-loss rate depend on the distance. And the distance also has implications for the determination of the birth place of ζ Pup.

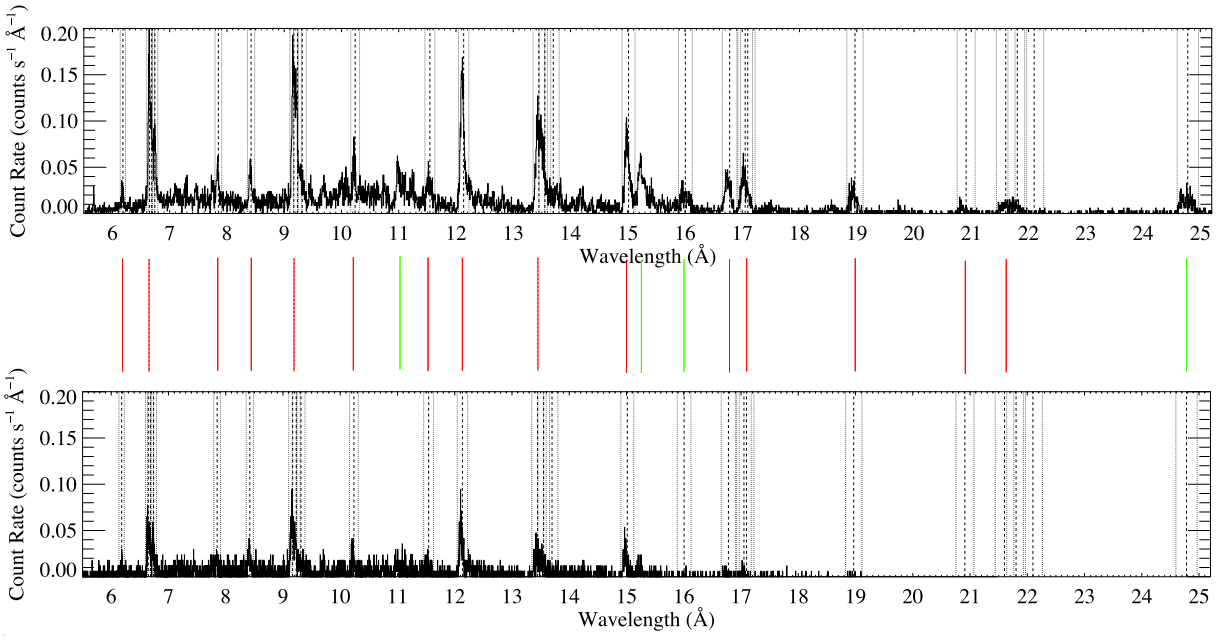

Figure 1. The entire usable portions of the MEG (top) and HEG (bottom) first order spectra of ζ Pup. The binning is native (2.5 mÅ for the HEG and 5 mÅ for the MEG). Vertical dashed lines in the data panels themselves represent the laboratory rest wavelengths of important lines. The lighter dotted lines on either side represent the Doppler shifts associated with the star's terminal velocity. Bold vertical lines between the two spectral plots indicate the lines we successfully fit with profile models (solid red) and lines we attempted to fit but which were too blended to extract meaningful model parameters (solid green). For all blended emission lines we show only one of these red or green lines, and align it with the bluest emission line in the blend.*Note to coauthors: This figure requires a few small changes, still.*

Table 1. Stellar and wind parameters adopted from Puls et al. (2006)

parameter	value
Sp. Type	O4 If
Mass[a]	53.9 $M_\odot$
$T_{\rm eff}$	39000 K
R_*	18.6 $R_\odot$
$v_{\rm rot}\sin i$[b]	230 km s^{-1}
v_∞	2250 km s^{-1}
β	0.9
$\dot{M}$[c]	8.3×10^{-6} $M_\odot$ yr^{-1}
$\dot{M}$[d]	4.2×10^{-6} $M_\odot$ yr^{-1}
$\dot{M}$[e]	1.5×10^{-6} $M_\odot$ yr^{-1}

[a] From Repolust et al. (2004).
[b] From Glebocki et al. (2000).
[c] Unclumped value from Puls et al. (2006).
[d] Also from Puls et al. (2006), but the minimum clumping model, in which the far wind, where the radio emission arises, is unclumped, but the inner wind, where the Hα is produced is clumped. Note that the methodology of Puls et al. (2006) only enables a determination to be made of the *relative* clumping in these two regions of the wind.
[e] From Bouret et al. 2008 (*Note to coauthors: This is from JC's Kauai poster; nothing seems to have appeared yet; J & J, you did this work with JC? And a paper is in the works?*), from detailed UV spectral modeling, assuming clumping.

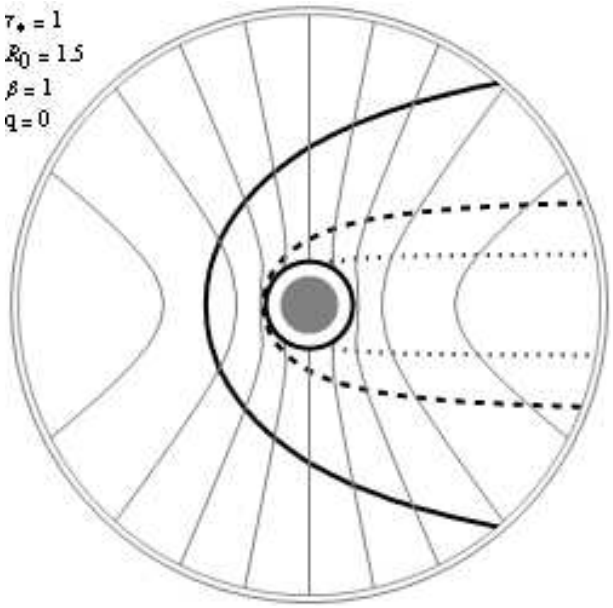

Figure 2. A visualization of the wind Doppler shift and optical depth – the two effects that govern the observed, broadened and asymmetric line shapes. The observer is on the left, and the light solid contours represent the line-of-sight velocity in increments of $0.2v_\infty$, with the blue shifts arising in the left hemisphere and the red shifts in the right. The star is the gray circle at the center, and the inner radius of the wind X-ray emission, R_o, is indicated at 1.5 R_* by the solid black circle. The solid heavy contour represents the locus of points with optical depth $\tau = 2$, and the dashed and dotted contours represent $\tau = 1$ and 0.5, respectively. The model parameters visualized here are nearly identical to those of the best-fitting model for the Mg XII Lyα line shown in Fig. 15. *Note to coauthors: We will clean this figure up a bit, removing the parameter labels in the upper left, incorporating them into the caption, and perhaps labeling some of the contours.*

3 THE EMISSION LINE PROFILE MODEL AND POROSITY

The non-porous model we fit to each line was first described by Owocki & Cohen (2001). It is a simple, spherically symmetric model that assumes that the local emission scales as the ambient density squared and that the many sites of hot, X-ray emitting plasma are statistically distributed throughout the wind above some onset radius, R_o, which is expected to be several tenths of a stellar radius above the photosphere in the LDI scenario (Feldmeier et al. 1997; Runacres & Owocki 2002). Attenuation of the emitted X-rays occurs in the bulk, cool ($T \approx T_{\rm eff}$) wind component via photoelectric absorption, mainly out of the inner shell of elements C through Si and also out of the L-shell ($n = 2$) of Fe. We assume that the atomic opacity of the cool wind, while a function of wavelength, does not vary significantly with radius. We further assume a beta-velocity law, $v = v_\infty(1 - R_*/r)^\beta$, for both wind components, with $\beta = 1$ and $v_\infty = 2250$ km s^{-1} as given by UV observations (Puls et al. 2006). The local velocity and density control the wavelength dependence of the emissivity, and the local optical depth governs the wavelength-dependent attenuation. These effects can be visualized in Fig. 2.

We cast the expression for the line profile first in spherical coordinates, with the origin at the center of the star and the observer at $z = \infty$. We integrate the specific intensity along rays of given impact parameter, and then integrate over rays. Integrating over the volume of the wind, we have:

$$L_\lambda = 8\pi^2 \int_{-1}^{+1} d\mu \int_{R_o}^{\infty} \eta_\lambda(\mu, r) r^2 e^{-\tau(\mu,r)} dr, \quad (1)$$

where L_λ is the luminosity per unity wavelength – it is the X-ray line profile. The angular coordinate $\mu \equiv \cos\theta$, η_λ is the wavelength-dependent emissivity that accounts for the Doppler shift of the emitting parcel of wind material (which is completely determined, under the assumptions of spherical symmetry and the velocity law, according to its location, (μ, r)). The emissivity also has a radial dependence due to the fact that it is proportional to the square of the ambient plasma density. The optical depth is given by τ. Its expression is more physically reasonable in cylindrical coordinates, as follows:

$$\tau(\mu, r) \equiv t(p, z) = \int_z^\infty \kappa\rho(r')dz', \quad (2)$$

where the dummy radial coordinate is given by $r' \equiv \sqrt{z'^2 + p'^2}$. The opacity, κ, does not vary significantly across a line (recall it is due to continuum processes – the strong wavelength dependence across a line profile arises purely from the geometry indicated in Fig. 2). Using the continuity equation and the beta-velocity law of the wind, we have:

$$t(p, z) = \tau_* \int_z^\infty \frac{\mathrm{R_* dz'}}{r'^2(1 - \mathrm{R_*}/\mathrm{r'})^\beta}. \quad (3)$$

We account for occultation of the back of the wind by the star by setting this optical depth integral to ∞ when $p < R_*$ and $z < \sqrt{R_*^2 - p^2}$. The constant at the front of eq. 3, $\tau_* \equiv \frac{\dot{M}\kappa}{4\pi \mathrm{R_* v_\infty}}$, is the fiducial optical depth and is equivalent to the optical depth value along the central ray, integrated down to the stellar surface, in the case where $v = v_\infty$. This quantity, τ_*, is the single parameter that describes the X-ray attenuation and governs the shifted and asymmetric form of the line profiles.

We note that the optical depth integral, while generally requiring numerical integration, can be done analytically for integer values of β. We use $\beta = 1$ throughout this paper (though we report on tests we did for non-integer β values in §4.2), and for that value of the parameter, the optical depth integral evaluates as:

$$t(p, z) = \frac{\mathrm{R_*}\tau_*}{z_*}(\arctan\frac{\mathrm{R_*}\mu'}{z_*} + \arctan\frac{z'}{z_*})_{z' \to z}^{z' \to \infty}, \quad (4)$$

where $z_* \equiv \sqrt{p^2 - R_*^2}$.

The intrinsic line profile function we assume for the emissivity at each location is a delta function that picks out the Doppler shift line resonance,

$$\eta \propto \delta(\lambda - \lambda_o(1 - \mu v(r)/c)). \quad (5)$$

This assumption is justified because the actual intrinsic line width is dominated by thermal broadening, which is very small compared to the Doppler shift caused by the highly supersonic wind flow.

Calculating a line profile model, then, amounts to solving equations 1 and 3 for a given set of parameters, R_o, τ_*, the normalization (which determines the value of η), and an

assumed wind velocity law, described by β and v_∞. This last parameter influences the emissivity term through its effect on the Doppler shift as a function of radius and spherical polar angle. And for our choice of $\beta = 1$, eq. 4 replaces eq. 3.

The model produces broad emission lines where the overall width, for an assumed wind velocity law, is governed by the parameter R_o. The closer to the star's surface R_o is, the more emission there is from low-velocity wind material, which contributes to the line profile only near line center. The larger R_o is, therefore, the broader the line profile. The value of τ_* affects the line's blue shift and asymmetry. The higher its value, the more blue shifted and asymmetric the profile. The interplay of the two parameters can be seen in figure 2 of Owocki & Cohen (2001).

A simple profile model that includes the effects of large-scale porosity was introduced by Owocki & Cohen (2006), and we adopt that model here and use it for the first time to quantitatively fit data. The key insight of that paper was that a single parameter describes the reduction in the effective opacity, in the presence of porosity. This parameter, the porosity length, $h \equiv \ell/f$, where f is the volume filling factor[2] of clumps, has already been briefly described in the introduction. In the case of significant porosity, where individual clumps are very optically thick, the effective opacity of the clump is simply its macroscopic cross section divided by its mass,

$$\kappa_{\rm eff} \equiv \frac{\ell^2}{m_{\rm c}} = \frac{\kappa}{\tau_{\rm c}}, \tag{6}$$

where

$$\tau_{\rm c} = \kappa \rho_{\rm c} \ell = \kappa < \rho > h. \tag{7}$$

Here κ is the atomic opacity, ℓ is the size scale of the clumps, $m_{\rm c}$, $\tau_{\rm c}$, and $\rho_{\rm c}$ are the mass, optical depth, and density of the clump, respectively, and $< \rho >$ is the radius-dependent average wind velocity (including the clumps and interclump medium, and assuming continuity, and so depends on $\dot{M}$, $\rm R_*$, and $v(r)$).

We assume that the porosity length itself is a function of radius, and a reasonable assumption (though not the one used in Owocki & Cohen (2006)) is that the porosity length scales with the local velocity,

$$h = h_\infty (1 - {\rm R_*/r})^\beta. \tag{8}$$

Note that this is equivalent to the parameterization of the "clump release frequency" employed by Oskinova et al. (2006), although we retain the porosity length formalism of Owocki & Cohen (2006) as it is more generalizable and also because using a length scale to describe the clumping facilitates comparisons to other determinations of clumping, especially from numerical simulations.

In order to better visualize the effects of porosity, we present a suite of realizations of porous winds in Fig. 3.

[2] We note that the filling factor is the reciprocal of the commonly used clumping factor, the square root of which represents the mass-loss rate correction factor when clumping is taken into account where it had previously been neglected. Put another way, the factor $1/\sqrt{f}$ represents the mass-loss rate overestimate if density-squared mass-loss diagnostics are used and clumping is neglected.

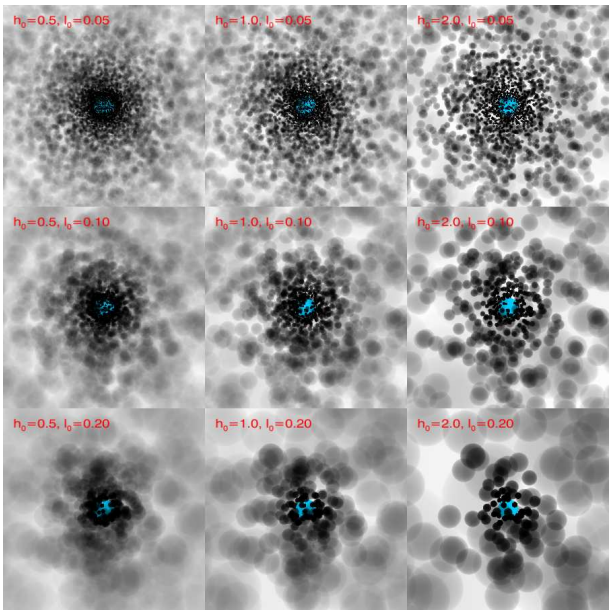

Figure 3. Monte Carlo realizations of clumpy and porous winds. The domain is a cube 20 $\rm R_*$ on a side. The star is shown at the center in blue. The projection is orthographic – parallel rays; no perspective size-distance cues. Small looking clumps are small because they are near the star. In these realizations, the clump scale is assumed to expand in proportion to its radial coordinate, maintaining a constant solid angle, as viewed from the star. The optical depth of the clump is indicated by its transparency or darkness. Columns in this figure have $h_\infty = 0.5, 1.0$, and 2.0 $\rm R_*$, from left to right. While rows have clump size scale $\ell = 0.05, 0.1$, and 0.2 $\rm R_*$, from top to bottom.

This array has three values of the terminal porosity length, $h_\infty = 0.5, 1.0$, and 2.0 $\rm R_*$, and three values of clump scale, $\ell = 0.05, 0.1$, and 0.2 $\rm R_*$. Only h_∞ affects the appearance of X-ray profiles. And indeed, the apparent transparency, in terms of the portion of the star and rear hemisphere that is visible in each panel, is greater for the realizations with higher values of h_∞, and independent of the clump scale. Note that because the filling factor, $f = \ell/h$, is constant along diagonals (upper left to lower right) in the figure, the mass-loss rate clumping correction factor for density-squared diagnostics is also constant along these diagonals. *Note to coauthors – especially Rich: How should we modify the figure and the associated discussion of porosity?*

The effective opacity is assumed to take the form,

$$\kappa_{\rm eff} = \frac{\kappa}{1 + \tau_{\rm c}}. \tag{9}$$

This "bridging law" connects the case of optically thin clumps ($\kappa_{\rm eff} = \kappa$) to that for completely optically thick clumps ($\kappa_{\rm eff} = \kappa/\tau_{\rm c}$). Using this definition of the effective opacity due to porosity, the optical depth integral becomes:

$$t(p,z) = \tau_* \int_z^\infty \frac{\rm R_* dz'}{(r'^2 + \tau_* h_\infty {\rm R_*})(1 - {\rm R_*/r'})^\beta}. \tag{10}$$

We fit this porous model to each line after fitting the non-porous model described at the beginning of this section. In Fig. 4 we show representative porous profile models. These show that the terminal porosity length, h_∞, has to exceed 1 $\rm R_*$ before porosity has significant effects on the

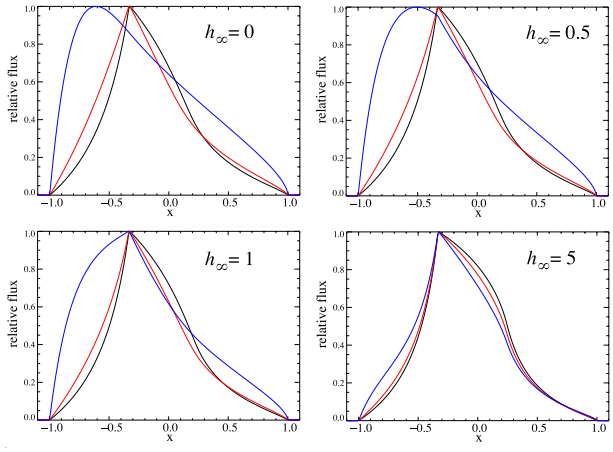

Figure 4. Line profile models that incorporate isotropic porosity. Each panel shows profiles with R_o = 1.5 R$_*$ and three different values of τ_*, τ_* = 1, 2, 8. The terminal porosity length increases from zero in the top left panel (so, these models are non-porous) to h_∞ = 5 R$_*$. Note that the effects of porosity are not significant until the porosity length is of order the stellar radius. These models are *not* convolved with the *Chandra* instrumental response; they are shown here at infinite resolution, and thus cannot be compared directly to the data.

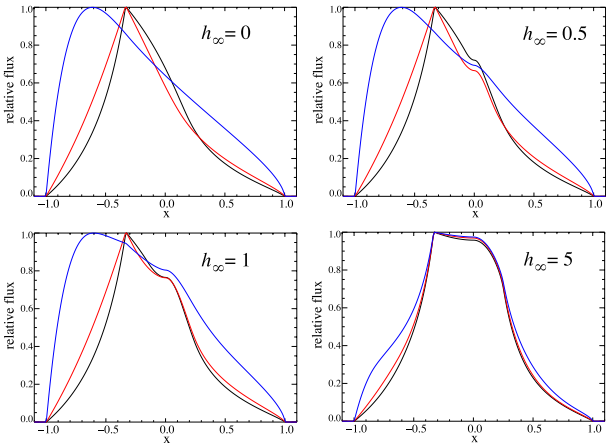

Figure 5. Line profile models that incorporate porosity from oblate clumps, aligned with the star's surface. Each panel shows profiles with R_o = 1.5 R$_*$ and three different values of τ_*, τ_* = 1, 2, 8. The terminal porosity length increases from zero in the top left panel (so, these models are non-porous) to h_∞ = 5 R$_*$. Note that here the effects of porosity are significant even when the porosity length is of order the stellar radius. Compare this figure to Fig. 4.

line profiles, but that for very large porosity lengths there is a fair amount of degeneracy between high porosity and low optical depth.

The third class of models we fit to the data follow the same formalism, including the description of the effect of porosity on the radiation transport via an effective opacity. Only now, we assume that clumps are oblate – flattened – and oriented so that their faces are parallel to the stellar surface. In this case, for optically thick clumps, the effective cross section is the projected cross section as seen from the observer's point of view. This simply amounts to modifying eq. 7 by a factor of μ,

$$\tau_c = \kappa\rho_c\ell/\mu = \kappa < \rho > h/\mu. \quad (11)$$

We then calculate the profiles from this expression for τ_c combined with equations 1, 2, and 9.

Porosity from oblate clumps, or shell fragments, is more efficient than porosity from spherical clumps. Smaller porosity lengths affect the profiles. The effect has a characteristic profile shape, with a bump on the sloping, redward wing near line center. This is the "Venetian blind effect" (Oskinova et al. 2006) that stems from the fact that it is those clumps that are on the sides of the wind, from the observer's point of view, that are seen edge-on, and have significantly enhanced photon escape. The associated lower effective opacity is at line center because the sides of the wind are traveling across the observer's line of sight and have small Doppler shifts. We show a suite of profile models in Fig. 5.

Note to coauthors: There's currently very little detail in the description of the porous models; especially the anisotropic porosity model. My assumption is that we (Maurice?) will write a short paper on the anisotropic porosity (oblate clump) model, and its properties. We will cite this reference, but will probably still have to add a bit more description here.

4 MODEL-FITTING PROCEDURE AND ANALYSIS

We describe the model-fitting technique in some detail and apply it to one representative strong line in the spectrum, Fe XVII at 15.014 Å, in the first subsection, and defer the discussion of the effects of various modeling assumptions and parameter choices to the second subsection.

4.1 Demonstration with one representative emission line

For each line in the spectrum, we first fit the non-porous (Owocki & Cohen 2001) profile model, described by equations 1 and 3 (really eq. 4 for $\beta = 1$), to the data. Note that this model has only three free parameters: the fiducial optical depth, τ_*, the minimum radius of X-ray emission, R_o, and the normalization of the line. After this, we fit the porous model with spherical clumps (Owocki & Cohen 2006), and lastly we fit the porous model with oblate clumps. These two porous models each have only one additional free parameter, the terminal porosity length, h_∞, described by eq. 8.

We begin the analysis procedure for each line by fitting the weak continuum in two regions, one to the blue side of the line and one on the red side (but excluding the wavelength range of the line itself). We assume the continuum is flat over this restricted wavelength region. We then fit the emission line over a wavelength range that is no broader than the line itself (and sometimes even narrower, due to blends with nearby lines, which can induce us to exclude contaminated portions of the line in question). The model we fit to each line is the sum of the empirical line profile model(s) we described in the previous section and the continuum model determined from the fit to the two spectral regions near the line. Note that the inclusion of the continuum does not introduce any new free parameters.

We fit the wind profile plus continuum model to both the MEG and HEG data (positive and negative first orders) simultaneously, if the HEG data are of good enough quality to warrant their inclusion (generally true only for lines with wavelengths shorter than about 16 Å), and to the MEG data only if they are not. We use the C statistic (Cash 1979) as the fit statistic. This is the maximum likelihood statistic for data with Poisson distributed errors, which these photon-counting X-ray spectra are. Note that the maximum likelihood statistic for Gaussian distributed data is the well-known χ^2 statistic, but it is not valid for these data, which have many bins with only a few counts, especially in the diagnostically powerful wings of the profiles.

We determine the best-fit model by minimization of the C statistic using the *fit* task in XSPEC. Once it is found, the uncertainties on each model parameter are assessed using the $\Delta\chi^2$ formalism[3] outlined in chapter 15 of Press et al. (2007), which is also valid for ΔC. We test each parameter one at a time, stepping through a grid of values (typically 36 by 36) and, at each step, refitting data while letting the other model parameters be free to vary. The 68 percent confidence limits determined in this manner are what we report as the formal uncertainties in the tables of fitting results in the next section. We also examine the confidence regions in two-dimensional sub-spaces of the whole parameter space in order to look for correlations among the interesting parameters.

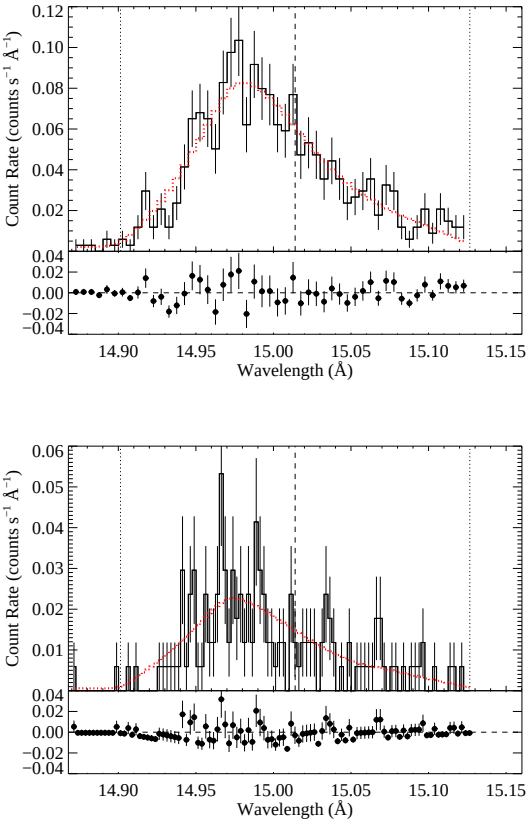

Figure 6. The Fe XVII line at 15.014 Å in the MEG (top) and HEG (bottom), with the best-fit non-porous model superimposed. We have not done any rebinning of the data. The error bars represent Poisson, root-N, statistics. The dashed vertical line indicates the laboratory rest wavelength of the emission line, and the two dotted vertical lines indicate the wavelengths associated with the Doppler shift due to the stellar wind terminal velocity of 2250 km s^{-1}. The model is shown as a (red) smooth histogram, while the data are shown as a (black) choppy histogram with error bars. The fit residuals are shown in the horizontal windows below the data.

We use the relatively strong and unblended Fe XVII line at 15.014 Å to demonstrate this fitting process. We show the MEG and HEG data for this line, along with the best-fit model (the set of model parameters, τ_*, R_o, and normalization that minimizes the C statistic) in Fig. 6. The best-fit model parameters are: $\tau_* = 1.97$, $R_o = 1.53$ R$_*$, and a normalization of 5.24×10^{-4} photons s^{-1} cm^{-2}. Using the ΔC criterion and testing each of these parameters one at a time, we find that the 68 percent confidence limits on the fit parameters are $1.63 < \tau_* < 2.35$, $1.38 < R_o/R_* < 1.65$, and $5.04 \times 10^{-4} <$ norm $< 5.51 \times 10^{-4}$. The confidence limits should be thought of as probabilistic statements about the

[3] This criterion is a specific numerical value of $\Delta C \equiv C_i - C_{min}$ for model realization i, where $C_{\rm min}$ is the C statistic value for the best-fit model.

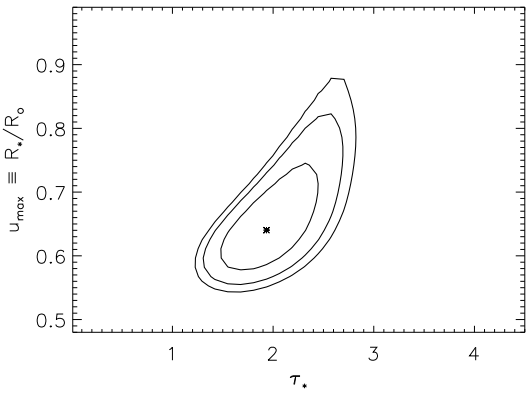

Figure 7. Confidence contours (68, 90, and 95 percent) for the non-porous model fitting of the the Fe XVII line at 15.014 Å. The best-fit, shown in Fig. 6, is represented by the asterisk. Note that we plot this, and all other confidence plots that involve the inner radius, R_o, in terms of u_{max}, or $u_o \equiv R_*/R_o$.

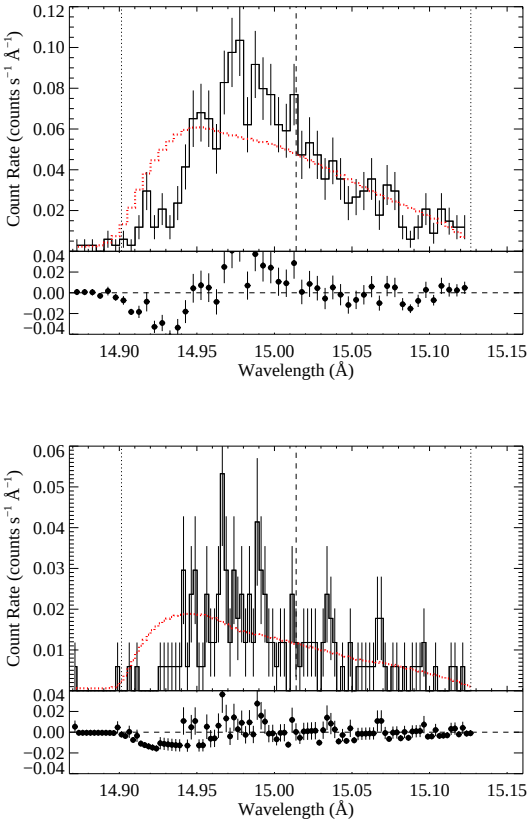

Figure 8. The Fe XVII line at 15.014 Å in the MEG (top) and HEG (bottom), with the best-fit non-porous model having $\tau_* = 8$ superimposed. This model fit is statistically unacceptable.

chance that the true parameter values lies withing the given range, given the physical assumptions of the model.

In Fig. 7 we show 68, 90, and 95 percent confidence limits in two-dimensional τ_*, R_o parameter space. *Note to coauthors: All the uses of the parameter u_{max} or u_o, especially in figures such as this one, will be removed. We will discuss everything in terms of R_o, and also remake all the 2-D confidence plots in τ_*,u_o space so they are displayed in τ_*,R_o space. This change will happen soon.* We calculate a grid of models, optimizing the other free parameters (just the normalization, in this case) at each point in the grid, and use values of $\Delta C = 2.30, 4.61, 6.17$ to define the extent of the confidence limits. Plots such as this one are a good means of examining correlations between model parameters, in terms of their abilities to produce similar features in the line profiles. We can see what the tradeoffs are between parameters in a quantitative way. For example, there is a slight correlation between u_o and τ_* evident in the figure. High values of u_o (R_o close to R_*), reduce emission on the line wing relative to the core (more emitting material at low velocity). So although high values of u_o (hot plasma as close as 1.2 R_*) are allowed at the 95 percent confidence limit, they require a large wind optical depth, $\tau_* \approx 3$, to compensate. High τ_* makes lines more blue-shifted and asymmetric, increasing the emission on the line wing relative to the core.

The value of τ_* expected from the traditional mass-loss rate and a model of the wind opacity at 15 Å is $\tau_* \approx 8$ (*Note to coauthors: The cmfgen opacity model we show in the discussion section implies a τ_* value closer to 7, but before redoing a bunch of fits, I'd like to make sure we're settled on the final version of our wind opacity model.*). The best-fit model with $\tau_* = 8$ is shown in Fig. 8. This model does not provide a good fit, having $\Delta C = 108$, implying rejection probabilities above 99.99 percent. This is the quantitative basis for claims that the X-ray emission lines of O stars in general, and ζ Pup in particular, are too symmetric and unshifted to be explained by the standard wind-shock scenario (Kahn et al. 2001; Cassinelli et al. 2001; Kramer et al. 2003).

After fitting the non-porous, Owocki & Cohen (2001) line profile model, we next fit a given emission line with the model that includes porosity from spherical clumps (Owocki & Cohen 2006), as given by eq. 10. This introduces an additional free parameter, h_∞. We repeat the process described above, finding the best-fit model by adjusting the free model parameters to minimize the fit statistic, assessing confidence limits on parameters individually, and then examining joint confidence limits on pairs of parameters.

For the Fe XVII line at 15.014 Å, we found that $h_\infty = 0.0$ was the best-fit value of the terminal porosity length. This is equivalent to a model without porosity (which is why we do not show a figure for this fit). The 68 percent confidence limit on this value is $h_\infty = 0.43$ R_* and the 90 percent confidence limit is $h_\infty = 1.07$ R_*. We can examine how this parameter interacts with the optical depth parameter, τ_*. In Fig. 9 we show the confidence contours in two-dimensional h_∞, τ_* parameter space. The correlation seen here between h_∞ and τ_* arises from the ability of porosity to reduce the effective opacity of the wind by hiding atomic opacity in optically thick clumps. And just as is expected theoretically (Owocki & Cohen 2006), the effect only becomes significant once the porosity length is is equivalent to the local radius (here, roughly 1.5 R_* and above, based on the fitted value of R_o). The confidence contours, enclosing parameter values that provide acceptable fits, show increasing correlation as h_∞ increases, but the effect of porosity on τ_* does not become significant until h_∞ is above 1 R_*. The strong effect of large h_∞ values and this parameter's strong correlation

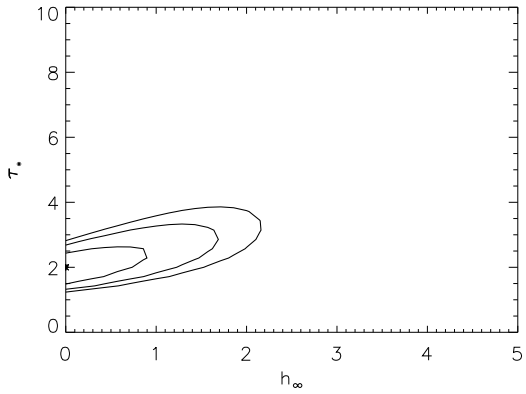

Figure 9. Confidence contours (68, 90, and 95 percent) for the porous model fitting of the the Fe XVII line at 15.014 Å. This porous model assumes spherical clumps, and the confidence contours show the joint distribution of h_∞ and τ_*. Note that we use the same axes ranges for all subsequent h_∞,τ_* confidence plots in order to facilitate easy comparisons.

with τ_* can be better seen in fits to noisier lines, with weaker constraints. The contours extend to higher h_∞ and τ_* values, and start to curve upward for $h_\infty > 1$ R$_*$, as can be seen in §4.

We have already shown that models with $\tau_* = 8$, the value implied by the traditional mass-loss rate, provide poor fits to this line. And even the 95 percent confidence region in the porous model fitting does not enclose any models with $\tau_* = 8$. However, we can still ask how large a value of h_∞ is required to accommodate this high value of τ_* expected from the traditional mass-loss rate. When we fit a model with $\tau_* = 8$ fixed and porosity included to reduce the effective optical depth of the wind, we find a best-fit value for the terminal porosity length of $h_\infty = 3.64$ R$_*$. We show this high τ_*, high h_∞ model in Fig. 10. Although this model cannot be rejected outright, it provides a worse fit to the data than does the non-porous model. The ΔC between these two models is $\Delta C \approx 15$, indicating that the non-porous model is preferred at the 99.9 percent confidence level. In other words, if the best-fit non-porous model is the correct model that completely describes the data, then there is only a 0.1 percent chance of obtaining a fit as poor as (*i.e.* with the same C statistic as) the one provided by the best-fit porous model due only to random error. This model has a noticeable bulge on the extreme blue wing as well as one near line center, which is where the agreement is the worst; in both places, there are many consecutive bins for which the model lies above the data. These two morphological features are characteristic of porous models (see Fig. 4) and ultimately prove to be the cause of the porous models' inability to provide better fits to the data than the non-porous models.

After fitting the porous model with spherical clumps, determining the best-fit model parameters, assessing the parameter confidence limits, and examining a model for which τ_* is fixed at the value implied by the traditional, literature mass-loss rate, we repeat the entire process for the porous model that assumes oblate clumps, as given by equation 11. For the representative Fe XVII line at 15.014 Å, we find a best-fit $h_\infty = 0.0$, just as we did for the porous model with

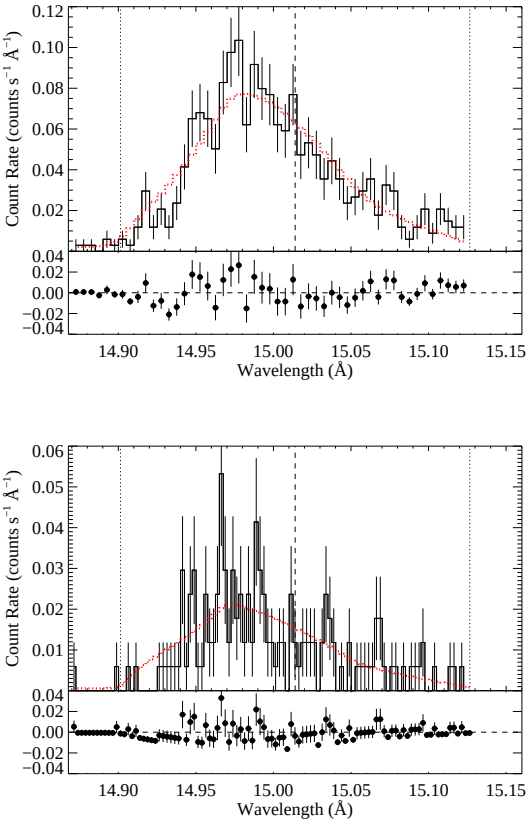

Figure 10. The Fe XVII line at 15.014 Å in the MEG (top) and HEG (bottom), with the best-fit porous model (with spherical clumps) having $\tau_* = 8$ superimposed. Compare to Fig. 6. Note that a very large porosity length, $h_\infty = 3.64$, is required to get a fit even this good.

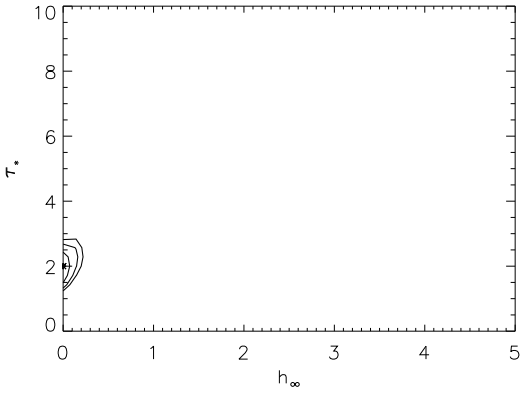

Figure 11. Confidence contours (68, 90, and 95 percent) for the porous model fitting of the the Fe XVII line at 15.014 Å. This porous model assumes oblate, or flattened, clumps, and the confidence contours show the joint distribution of h_∞ and τ_*.

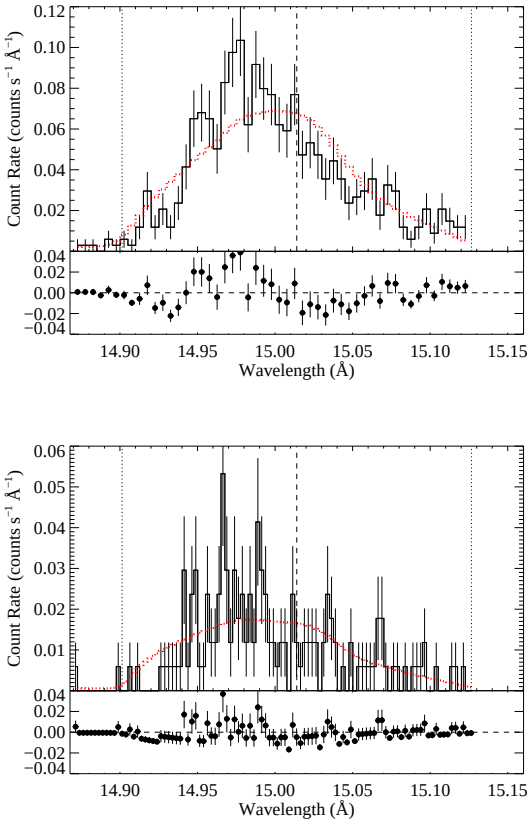

Figure 12. The Fe XVII line at 15.014 Å in the MEG (top) and HEG (bottom), with the best-fit porous model (with flattened clumps) having $\tau_* = 8$ superimposed. The best-fit value of the terminal porosity length, for the model shown here, is $h_\infty = 1.59$ R$_*$. Compare this model fit to Fig. 6 and Fig. 10.

spherical clumps. In other words, the non-porous model is preferred over the porous model with flattened clumps (and again, we do not bother to show this model, because it is functionally identical to the one shown in Fig. 6). When we test the confidence limits on the model parameters, we find the same limits we found for the non-porous model fits, at 68 percent confidence. This means that allowing for porosity from flattened clumps does not improve the fit quality for any combination of other parameters. When we evaluate the confidence limits on h_∞ itself, we find a 68 percent upper limit of only $h_\infty = 0.04$ R$_*$, and a 90 percent upper limit of 0.10 R$_*$. So, even modest values of the terminal porosity length in the context of porosity from flattened clumps make the fits significantly worse. In Fig. 11 we show the joint h_∞,τ_* confidence limits. And in Fig. 12 we show the best-fit porous model assuming flattened clumps but with the optical depth parameter, τ_*, fixed at the value implied by the literature mass-loss rate, $\tau_* = 8$. The fit is very poor – much worse than that provided by the porous model with spherical clumps. The terminal porosity length required even to achieve a fit of this dubious quality is $h_\infty = 1.59$ R$_*$.

4.2 Sensitivity of fitting results to modeling assumptions

We have made various assumptions and choices in carrying out the line-profile modeling, as described in the previous subsection. And we therefore have investigated many of these, again using the Fe XVII line at 15.014 Å as a test case. In this subsection, we report on the sensitivity of our results to the following assumptions and choices: background subtraction; determination of the continuum level; exclusion of portions of the line due to possible blending; inclusion of the weak HEG data; the adopted values of β and v_∞ for the wind; whether to allow the X-ray volume filling factor to vary with radius (as parameterized by q in $f \propto r^{-q}$ – see Owocki & Cohen (2001)); and for porous models, the form of the bridging law that describes how the effective opacity behaves as optically thin clumps make the transition to optical thickness. We will very briefly describe those factors that we found to be unimportant, and discuss in a little more detail those that did make a difference. The base-line model fitting we describe is the non-porous modeling described in the previous subsection, except that we fit only the MEG data for the 15.014 Å line.

We examined the default background spectra, which were very low, and also experimented with fitting the 15.014 Å line with and without the background subtracted and found almost no difference. We therefore opt to neglect the background when fitting each of the lines in the spectrum. The sensitivity to the continuum fit is a little greater, but still nearly negligible. When we changed the continuum level by a factor of two, none of the parameter values changed by more than ten percent (*Note to coauthors – especially Maurice: Should we look at what happens when we completely ignore the continuum? This would facilitate comparison with Kramer et al. (2003).*). Some lines in the spectrum are blended with weaker lines. The cleanest way to handle this situation is to exclude the contaminated bins from the modeling. To test the effects of this, we eliminated 0.03 Å from the red wing of the 15.014 Å line and refit the data. We then repeated this experiment eliminating 0.07 Å - leaving only about two-thirds of the data. Even in this second, extreme case, the fit parameters varied by less than ten percent and the confidence regions only expanded slightly.

For most lines, the HEG data is significantly weaker than the MEG data. We find for the 15.014 Å line that including the HEG data changes the best-fit model parameters by, at most, a few percent, but it does tighten the confidence limits somewhat. The effect of including the HEG data is more significant for the shorter wavelength lines, where the effective area of the HEG is larger. There is very little penalty for including the HEG data, so we do so for all lines shortward of 16 Å. We also fit the MEG and HEG data separately for the 15.014 line to verify that there are not systematic effects between these two spectra; and there are not. The separate fits give results that are very similar to each other, with significantly overlapping 68 percent confidence limits for all parameters.

The original Owocki & Cohen (2001) line profile model allows for a radially varying filling factor of X-ray emitting plasma, parameterized as a power law function of radius. Values of the power-law index, q, that differ significantly from zero (no radial variation) can cause changes in the line

profiles that are not insignificant, effectively weighting the emission from parts of the wind according to their velocity (via the beta-velocity law relationship between velocity and radius). However, we find that when we allow q to be a free parameter the best-fit value is generally very close to zero. For the representative 15.014 line, it is $q = -0.09$, and $q = 0$ is included in the 68 percent confidence region. The general result is consistent with that found for this and other stars (Kramer et al. 2003; Cohen et al. 2006). Thus, to keep the number of free parameters manageable, we fix $q = 0$.

The factors discussed above have a very minor influence on the results of the line fitting. However, the remaining factors can have a significant effect.

The velocity-law exponent, β, affects line profiles for two reasons: (1) the velocity law affects the mapping between radius and Doppler shifted wavelength, and so affects the emission profile; and (2) via the continuity equation, it affects the density and so affects both the emission and the absorption. Indeed, for our representative emission line, when we change the value of β from 1 to 0.8, both τ_* and R_o change by 10 to 20 percent. The determinations of β for ζ Pup vary from at least 0.9 to 1.15, and so using a value of $\beta = 1$ seems reasonable, especially as it speeds the calculation of the line profile model by allowing the optical depth integral to be done analytically, so we will use that value. If, in the future, a new and more accurate determination of β is made, and it differs significantly from $\beta = 1$, then the results reported in this paper can be scaled accordingly. We also note that the X-ray emitting plasma and the bulk wind that attenuates the X-rays may not necessarily be described by the same beta velocity law. However, there is no independent evidence for this, and with the short post-shock cooling lengths expected in the relatively dense wind of ζ Pup, the X-ray emitting plasma in the wind is more likely to have a velocity close to the ambient wind velocity[4]. And furthermore, the observed X-ray emission line widths in ζ Pup and other early O supergiants are completely consistent with the β and v_∞ values inferred from UV and optical spectroscopy of these stars.

The terminal velocity of ζ Pup is relatively well established, with reasonable estimates from several different groups that vary by about ± 10 percent about our adopted value of 2250 km s^{-1}. However, when we explored the effect of varying the terminal velocity in our fitting of non-porous wind profile models to the 15.014 Å line, we found that the value of τ_* was quite sensitive to the assumed wind terminal velocity, even within this relatively narrow range. This can be understood because the blue shift of the line centroid in the dimensionless, scaled wavelength parameter, $x \equiv (\lambda/\lambda_o - 1)c/v_\infty$, depends directly on the degree of wind absorption. The same observed profile appears more blue shifted in scaled wavelength units if the terminal velocity is (assumed to be) smaller. Our tests with the 15.014 Å line show that the best-fit value for τ_* ranges from 2.16 to 1.35 when we use terminal velocities between 2200 km s^{-1} and 2485 km s^{-1}. This variation is larger than that caused by every other parameter uncertainty and assumption we have explored. Thus, while we consider the value of $v_\infty = 2250$ km s^{-1} to be quite reliable, future re-assessments of this parameter will necessitate a rescaling of the optical depth, and mass-loss rate, results we report in this paper.

For porous models, there are at least two opacity "bridging laws" that span the limit between optically thin and thick clumps ($\kappa_{\rm eff} = \kappa$ to $\kappa_{\rm eff} = \ell^2/m_{\rm c} = \kappa/\tau_{\rm c}$), given by equations (4) and (6) in Owocki & Cohen (2006). We call these the "exponential"($\kappa_{\rm eff}/\kappa = (1-e^{-\tau_c})/\tau_c$) and "Rosseland" ($\kappa_{\rm eff}/\kappa = (1/(1+\tau_c))$) bridging laws. We fit the 15.014 Å line (both MEG and HEG) with (spherical clump) porosity models, using both bridging laws. We found a roughly 30 percent difference in the terminal porosity length, h_∞, required to fit the data when τ_* was fixed at a high value, in the sense that the exponential form of the effective opacity requires larger porosity lengths and the Rosseland form requires smaller ones. The Rosseland model provides a modestly better fit than the exponential one. We use the Rosseland form throughout this paper for both types of porous model fits (spherical clumps and oblate clumps).

[4] X-ray emitting plasma is too highly ionized to be effectively driven by the photospheric UV radiation field. However, for small enough parcels, the ram pressure of the surrounding wind should keep the post-shock, hot plasma moving at the ambient velocity.

5 RESULTS OF THE LINE PROFILE MODEL FITTING

Note to coauthors: Only 12 of the 14 lines are included in the plots shown right now. The other two will be added soon, but won't change the results.

We repeated exactly the process described in the previous section for fitting non-porous and then two types of porous models to every emission line in the spectrum of ζ Pup, as indicated in Fig. 1. In cases where lines of relatively comparable strength are blended, we generally fit the multiple lines simultaneously. In several cases, including Ne X Lyα, we excluded a portion of the line because of possible blending with an iron line. For shorter wavelength helium-like line complexes, we fit the components simultaneously, with model parameters tied together (and the alteration of the profiles of the forbidden and intercombination lines by the UV photoexcitation of the excited hot ions self-consistently accounted for). For oxygen, though, where the spectral resolution is highest and the resonance scattering may affect the resonance line, we report fits for only the intercombination line (*Note to coauthors: This is not yet the case, and it may prove impossible to isolate the intercombination line, due to blending; I'm still working on it.*). For several lines, including N VII Lyα, contamination, or blending by strong lines with uncertain relative intensities (N VI Heβ in the case of N VII Lyα) makes it impossible to reliably constrain the model parameters. Altogether we obtain reliable and interesting results from 14 emission lines or line complexes. Some of these do not provide meaningful constraints when we fit the non-porous models, with their additional parameter, and so we report on results for somewhat fewer lines in those cases.

5.1 Non-porous model fitting results

For the non-porous model fits, we list the best-fit parameters and confidence limits in Table 2 and graphically summarize the results for τ_* and R_o in Figures 13 and 14. There appears to be a trend in the optical depth values, which we will discuss in the following section. We show fitting results from three more important emission lines, which clearly demonstrate the correlation between τ_* and wavelength. The shortest wavelength line with the tightest constraints in the Lyα line of Mg XII at 8.421 Å, which we show – both the MEG and HEG data along with the simultaneous best-fitting model – in Fig. 15. That figure also shows the jointly constrained τ_* and R_o confidence limits. We show similar figures for the medium wavelength Ne X Lyα line in Fig. 16 and the longer wavelength O VIII Lyα line in Fig. 17.

Note to coauthors: We could spend a paragraph discussing the characteristics of these fits: some correlation between τ_* and u_o, as discussed in the previous section for the iron line at 15.014 Å; lack of very firm constraints on R_o (u_o). I'm not sure we need to go beyond what we've already said, though.

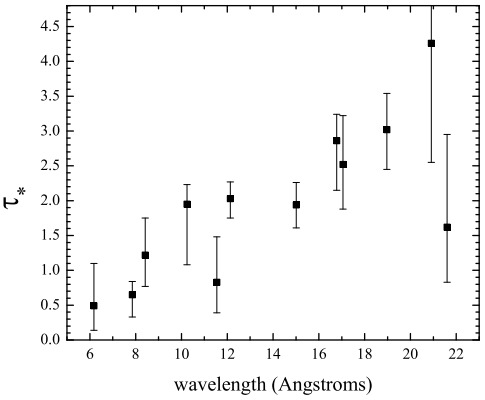

Figure 13. Values of τ_* derived from the non-porous model fits, shown with their 68 percent confidence limits. Line complexes and blends that were fit with multiple model components are represented by only one point.

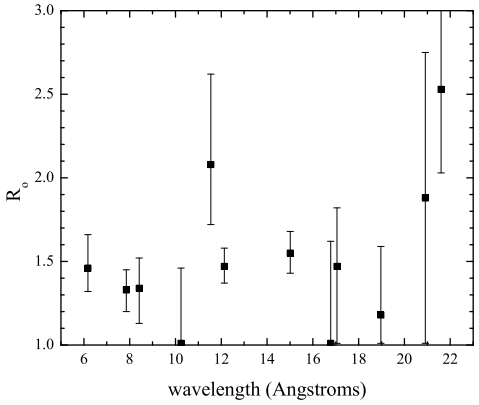

Figure 14. Values of R_o derived from the non-porous model fits, shown with their 68 percent confidence limits. Line complexes and blends that were fit with multiple model components are represented by only one point.

Table 2. Non-porous model fits

ion	wavelength (Å)	τ_*	R_o (R_*)	normalization (10^{-5} ph cm^{-2} s^{-1})
Si XIV	6.1822	$0.49^{+.61}_{-.35}$	$1.46^{+.20}_{-.14}$	$0.77^{+.11}_{-.14}$
Mg XI	7.8503	$0.65^{+.19}_{-.32}$	$1.33^{+.12}_{-.13}$	$1.33^{+.17}_{-.13}$
Mg XII	8.4210	$1.22^{+.53}_{-.45}$	$1.34^{+.18}_{-.21}$	$2.95^{+.24}_{-.24}$
Ne X	10.2388	$1.95^{+.28}_{-.87}$	$1.01^{+.45}_{-.00}$	$2.99^{+.31}_{-.29}$
Ne IX	11.5440	$0.83^{+.65}_{-.44}$	$2.08^{+.54}_{-.36}$	$5.00^{+.40}_{-.50}$
Ne X	12.1339	$2.03^{+.24}_{-.28}$	$1.47^{+.11}_{-.10}$	$26.9^{+1.1}_{-.7}$
Fe XVII	15.014	$1.94^{+.32}_{-.33}$	$1.55^{+.13}_{-.12}$	$52.4^{+2.5}_{-1.6}$
Fe XVII	16.780	$2.86^{+.38}_{-.71}$	$1.01^{+.61}_{-.00}$	$23.1^{+1.9}_{-1.2}$
Fe XVII[a]	17.051, 17.096	$2.52^{+.70}_{-.64}$	$1.47^{+.35}_{-.46}$	$17.2^{+0.9}_{-1.1}$, 15.5
O VIII	18.969	$3.02^{+.52}_{-.57}$	$1.18^{+.41}_{-.17}$	$37.0^{+2.8}_{-2.6}$
N VII	20.9099	$4.26^{+2.28}_{-1.71}$	$1.88^{+.87}_{-.87}$	$14.8^{+2.3}_{-1.9}$
O VII[b]	21.602, 21.804	$1.62^{+1.33}_{-.79}$	$2.53^{+.85}_{-.50}$	$31.9^{+4.0}_{-3.9}$, $28.0^{+2.9}_{-3.8}$

[a] We fit these two blended lines simultaneously, with a fixed normalization ratio of 0.9. Both line profile components were forced to have the same τ_* and R_o values.

[b] In this case, while the two components' τ_* and R_o parameter values were tied together, the two normalizations were free to vary independently.

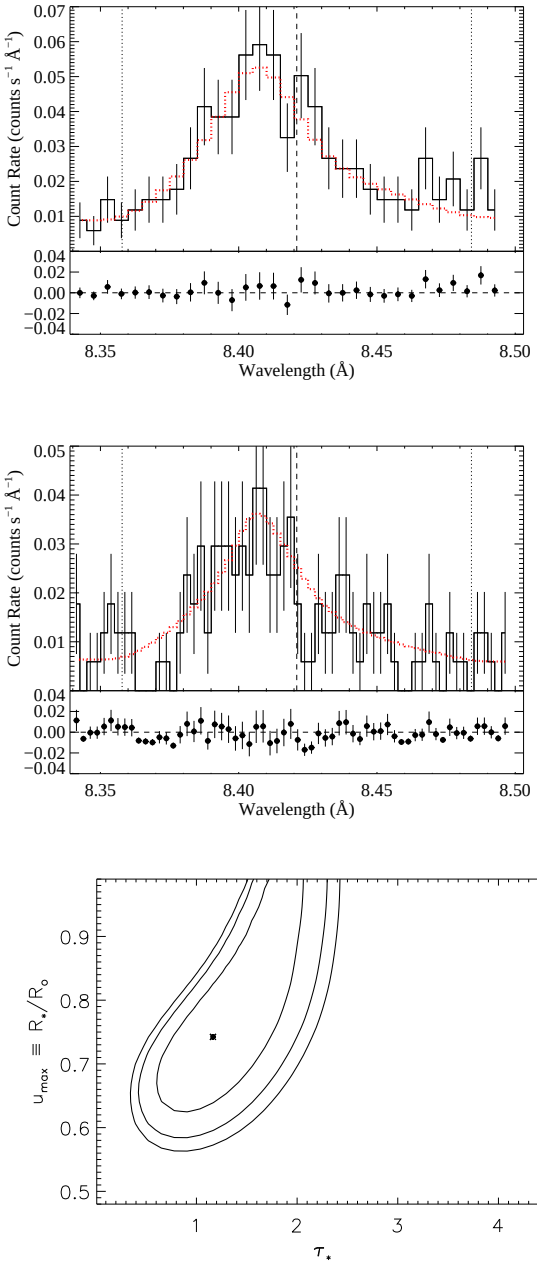

Figure 15. The MEG (top) and HEG (middle) measurements of the Mg XII Lyα line at 8.421 Å. This line shows a relatively small degree of blue shift and asymmetry, indicative of a low τ_* value, as is expected at short wavelengths, where the wind opacity is smaller. We also show the 68, 90, and 95 percent confidence limits in τ_*, u_o parameter space (bottom).

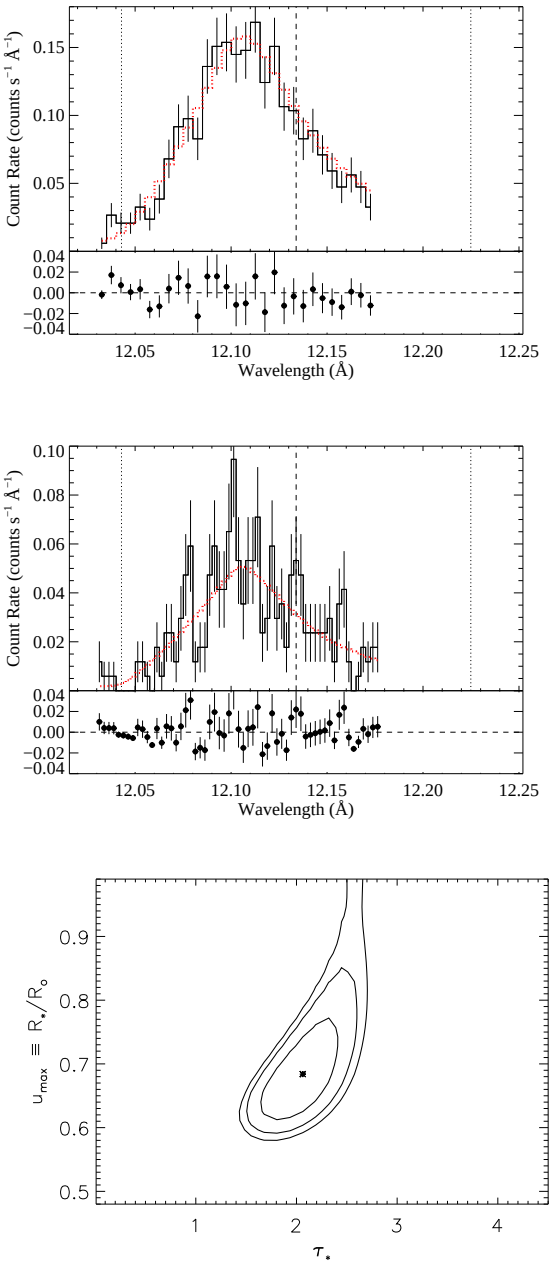

Figure 16. The MEG (top) and HEG (middle) measurements of the Ne X Lyα line at 12.134 Å. This line shows an intermediate degree of blue shift and asymmetry, indicative of an intermediate τ_* value, as is expected at its wavelength, where the wind opacity is larger than at the wavelength of the Mg XII Lyα line, but not as large as at longer wavelengths. We also show the 68, 90, and 95 percent confidence limits in τ_*, u_o parameter space (bottom).

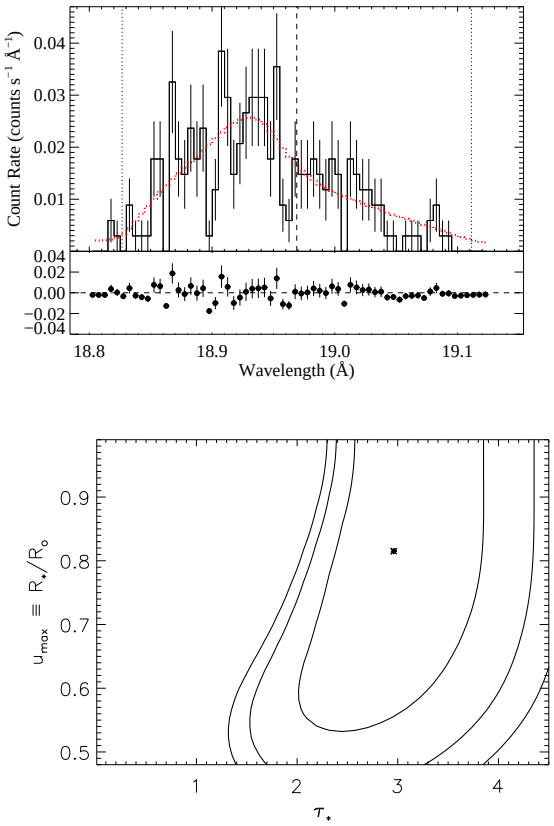

Figure 17. The MEG (top) measurements of the O VIII Lyα line at 18.969 Å. This line shows a relatively large degree of blue shift and asymmetry, indicative of a higher τ_* value, as is expected at longer wavelengths, where the wind opacity is larger. We did not include the very weak HEG data in the analysis of this line. We also show the 68, 90, and 95 percent confidence limits in τ_*, u_o parameter space (bottom).

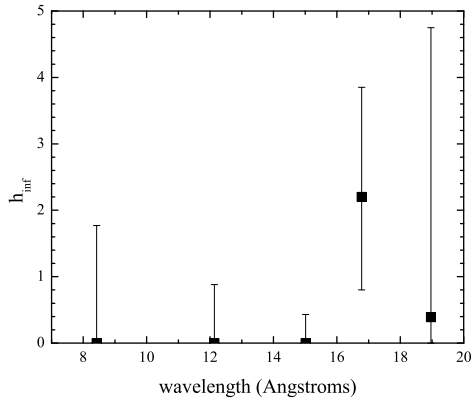

Figure 18. For the emission lines where a meaningful constraint can be put on the porosity length from the model fitting (that assumes spherical clumps), we show the best-fit and 68 percent confidence limits on the terminal porosity length, h_∞, in units of R_*.

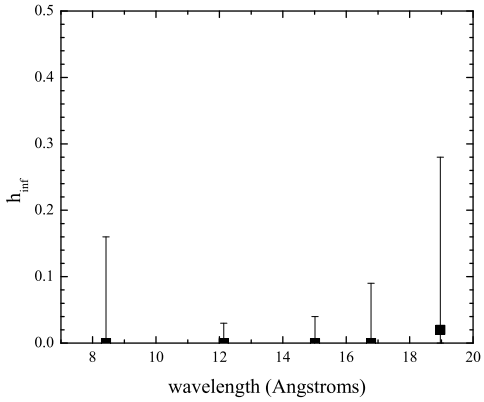

Figure 20. For the emission lines where a meaningful constraint can be put on the porosity length from the model fitting (that assumes oblate clumps), we show the best-fit and 68 percent confidence limits on the terminal porosity length, h_∞, in units of R_*.

5.2 Porous model fitting results with spherical clumps

For the fits of porous models that assume spherical clumps, we generally find – as we did for the demonstration line at 15.014 Å – that porosity lengths of zero ($h_\infty = 0$) are preferred. In Fig. 18 we show the best-fit values of h_∞ and their individual 68 percent confidence limit error bars. Note that for the line at 16.78 Å, the value of $h_\infty = 0$ is easily enclosed by the 90 percent confidence limits (and even by the 68 percent confidence limits, when they are jointly computed between h_∞ and τ_* as shown in the third panel on the left in Fig. 19). So, these data are all consistent with $h_\infty = 0$. However, of course, some degree of porosity generally is also consistent with each of these lines. In this subsection, we show the 68 percent upper limits to the terminal porosity length parameter, h_∞, for each line that is strong enough to warrant fitting with these models. We also examine the trade-off between h_∞ in τ_*, both by looking at the joint probability distributions of these two key parameters, and by fitting models to several of the stronger lines for which we fix the value of τ_* at that implied by the traditional, unclumped mass-loss rate of 8.3×10^{-6} $M_\odot$ yr^{-1}.

In Fig. 19 we show the joint confidence limits on h_∞, τ_* for eight lines. Only the Fe XVII line at 15.014 Å, which we have shown already in the previous section, the Ne X Lyα line at 12.134 Å, and the Mg XII Lyα line at 8.421 Å provide relatively tight constraints on h_∞ and τ_*. The other, weaker or blended lines provide more modest constraints, and generally allow for any value of h_∞, provided τ_* is high enough.

These confidence regions in h_∞, τ_* parameter space enable us to quantitatively examine the trade-offs between the two parameters and, thus, between lower mass-loss rates and significant wind porosity. We have already shown in the previous section that for the Fe XVII line, the value of the fiducial optical depth implied by the traditional mass-loss rate, $\tau_* = 8$ is not only disfavored compared to models with little or no porosity, (i.e. it lies outside the 95 percent confidence region) but that such high optical depth models require very large porosity lengths ($h_\infty = 3.64$ R_*, for this line). The same is true of the other higher signal-to-noise, unblended lines. We can assess this quantitatively by noting the minimum value of h_∞ for which a given confidence level intersects the τ_* value implied by the assumed mass-loss rate. Given the wind opacity model we discuss in the next section, the traditional mass-loss rate of ζ Pup implies a value of $\tau_* = 4$ for the Ne X line at 12.134 Å, and a value of $\tau_* = 10$ for the O VIII line at 18.969 Å, for example. The 90 percent confidence limit contour intersects these values of τ_* at $h_\infty \approx 1.3$ R_* for both of these lines. Even lines that are quite poorly constrained overall, such as the Fe XVII lines at 16.780 Å and the blend near 17 Å, require terminal porosity lengths of $h_\infty > 1$ R_* for model fits that are adequate.

We also fit high τ_* models, with that parameter fixed at the value implied by the traditional mass-loss rate. *Note to coauthors: We still have to make this figure and write a short paragraph. The emphasis will be on the very high values of h_∞ that are required to accommodate the high values of τ_* expected from the literature mass-loss rates; not on the fit quality of these high optical depth, high porosity length model fits.*

5.3 Oblate clump porous model fitting results

We perform similar tests on the data using the porous model that assumed oblate clumps. in general, we find even worse fits than for the spherical clump porosity modeling. In every case but one, porosity lengths of zero are preferred, and in the other case, a value of $h_\infty = 0.02$ R_* gives the best fit, but any value on $0.0 < h_\infty < 0.28$ R_* is allowed at the 68 percent confidence level. Even very modest values of the porosity length are rejected for oblate clumps in the case of Ne X Lyα as well as the Fe XVII line at 15.014 Å and blend near 17.1 Å. We show the fitting results as a scatter plot of best-fit h_∞ values with error bars in Fig. 20 and show the confidence contours in h_∞, τ_* space in Fig. 21.

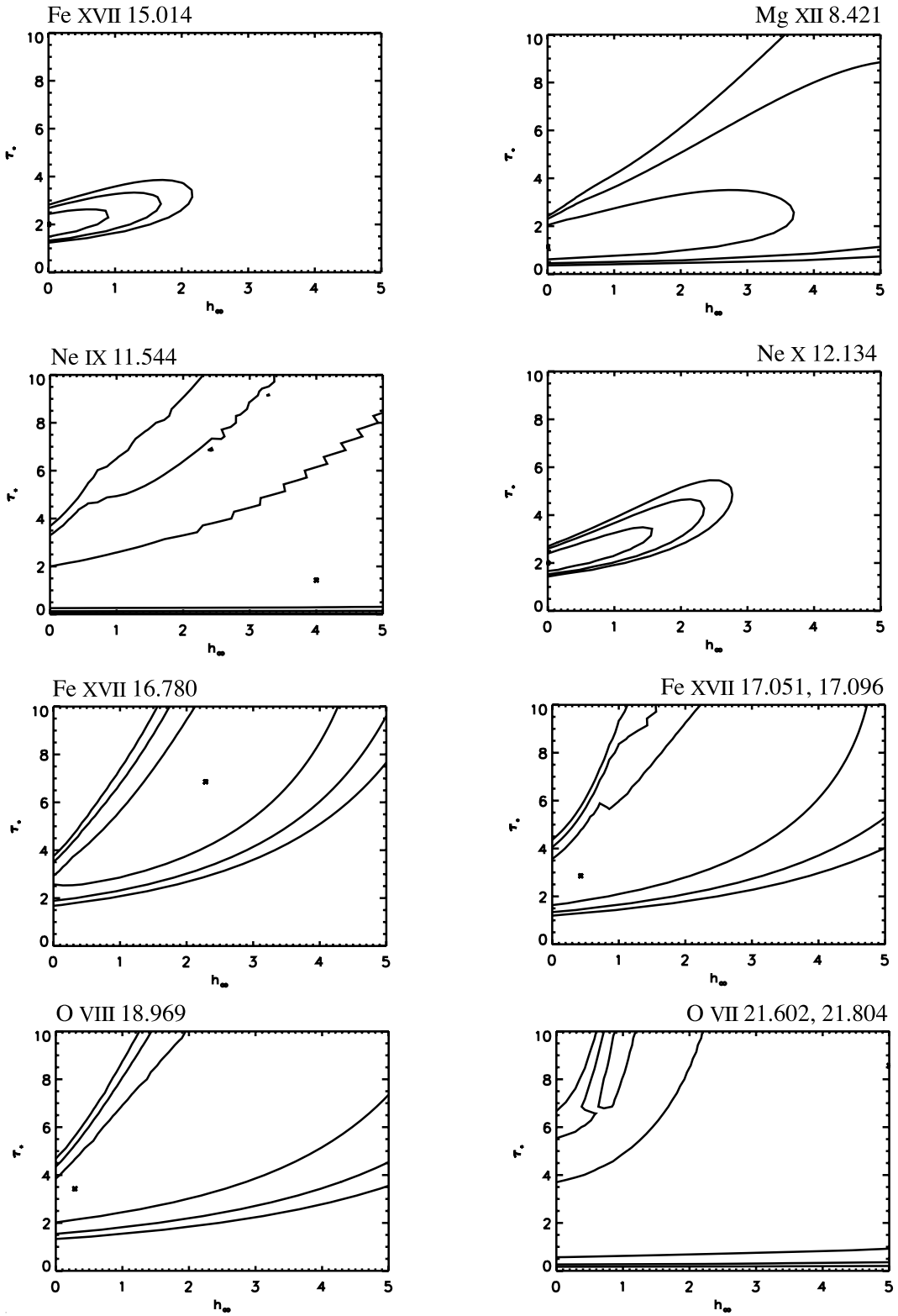

Figure 19. The joint h_∞, τ_* 68, 90, and 95 percent confidence regions for fits of porous models assuming spherical clumps to the strongest lines in the *Chandra* spectrum of ζ Pup. The best-fit models are indicated by the asterisks. Note that for the higher signal-to-noise lines, a value of $h_\infty = 0$ tends to be preferred, although significantly larger values are allowed. And for the lower signal-to-noise lines, even if higher values are marginally preferred, a value of $h_\infty = 0$ is allowed at the 68 percent confidence limit in every case.

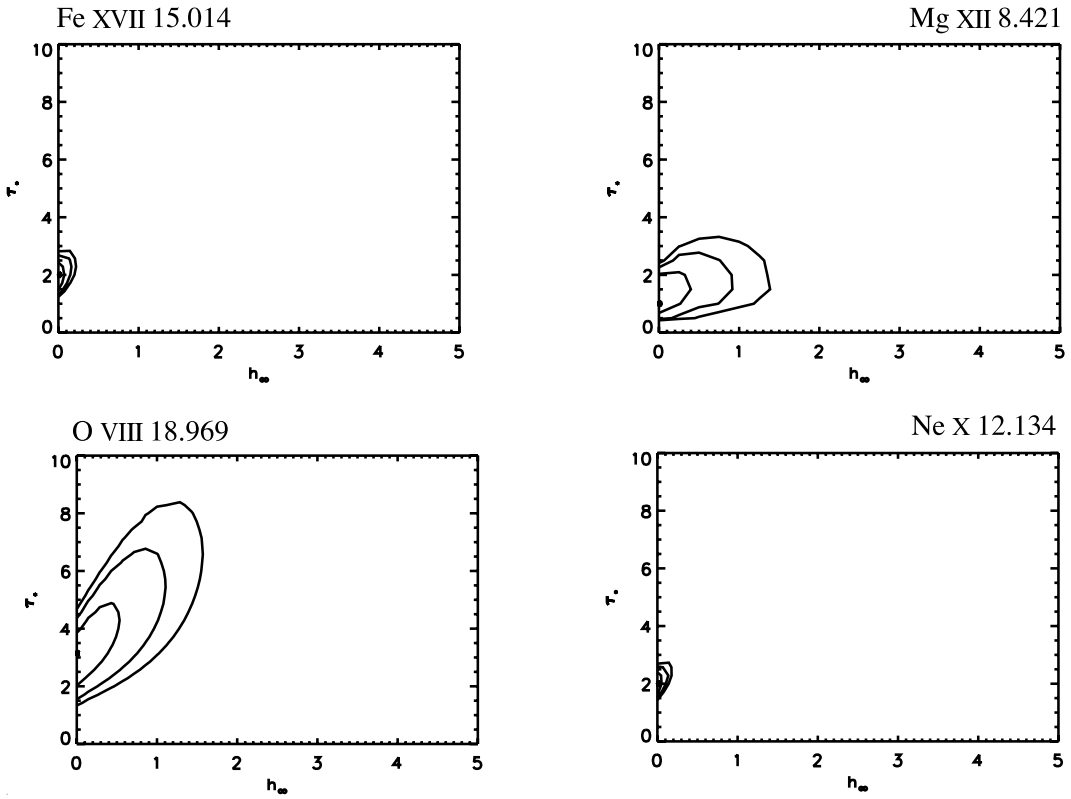

Figure 21. The joint h_∞, τ_* 68, 90, and 95 percent confidence regions for fits of porous models assuming oblate clumps to the strongest lines in the *Chandra* spectrum of ζ Pup. The best-fit models are indicated by the asterisks. Note that the constraints are much tighter than for the porous models that assume spherical clumps. In every case, $h_\infty = 0$ is preferred. *Note to coauthors: We have to add the Fe XVII line at 17 A to this figure.*

Note to coauthors: We have to write a paragraph and show a figure demonstrating the poor fits provided by high τ_*, high h_∞ models, with τ_* fixed by the traditional mass-loss rate.

Note to coauthors: Feedback on the figures showing the 2-D confidence regions (τ_*,h_∞) would be appreciated. We can show fewer of these for the spherical clump model. I can remake some of the figures with finer grids so the contours are smoother. But maybe it's not worth showing all these. On the flip side, I could add a plot for the 16.78 Å line to the suite of contour plots for the oblate clump modeling.

In summary, the porous models do not provide significantly better fits to any of the data than do the non-porous models. And for the highest quality data, the porous models provide worse fits. This is especially true for the porous models based on oblate clumps. When porosity is allowed, the values of the porosity length that are required to provide adequate fits to the data are very large – always in excess of $h_\infty = 1$ R$_*$ for models with spherical clumps.

6 DISCUSSION AND IMPLICATIONS OF RESULTS

Note to coauthors: Thus far we have just an outline.Input would be welcome.

Basic conclusions - non-porous: R_o in line with LDI predictions and a traditional beta law for the emitting plasma; Wind attenuation significant (as found by Kramer et al. 2003) and there is a wavelength trend in τ_*.

We will quantify the mass-loss rate based on our taustar values and a model of the wind opacity. This will entail introducing the wind opacity model, supplied by John and Janos, and shown in Fig. 22. We can list the opacity values for various lines, emphasizing the importance of using detailed opacities (e.g. the trend is surprisingly flat for $\lambda > 10$ Å; due mostly to the O underabundance and N overabundance). And using this model of the wind opacity, we can derive the mass-loss rate, as shown in Fig. 23. The wavelength trend argues against porosity, which corresponds to the dashed line in Fig. 23. Note two things: (1) we will discuss the effect of resonance scattering, which will tend to push a few of the longer wavelength τ_* points up. And (2) it's possible that the readjustment of our opacity model (inclusion of other elements; reassessment of the abundances) will push the model up somewhat, perhaps especially at shorter wavelengths.

We will also want to discuss the uncertainties on the mass-loss rate determination that stem from uncertainties in the abundances.

Emma has done a simultaneous fit to all strong lines. She gets results (including $\dot{M} = 3.3 \times 10^{-6}$ $M_\odot$ yr^{-1}) very similar to what we find from the analysis of the fits to the individual lines. We will mention this, too. She finds a single model provides an adequate fit to all the lines, simultaneously.

We can discuss the R_o trend or lack thereof. No strong evidence is found for different emitting ions arising at different radii. The purported trend, based primarily on f/i ratios, others have found is an absorption effect (they mostly claim, and I agree). We should emphasize that Joe, Lida and others were right to note that the emergent photons tend to arise near R_1 and point out (1) our wavelength-dependent τ_* values support this claim and (2) that our lower mass-loss rate does not lead to a problem with R_1 moving inward because when you treat the f/i ratios correctly, and don't assume that they form at a single radius, the inner radius of their formation moves inward also.

Basic conclusions – porosity: The wavelength dependence of τ_*, measured here for the first time, puts important limits on porosity.

The fits to individual lines also argue against porosity. It generally can't be ruled out but (1) never is required and provides worse fits than do the non-porous models, and (2) the values of porosity length required to make a difference are unrealistically high. (We can note – and I can make a figure, and annotated version of the h_∞,τ_* confidence contour plot – that (Oskinova et al. 2006)'s assumed value of $h_\infty = 1$ R_* has a negligible effect on the profiles (for spherical clumps). We can also bring in Luc's simulations here. In fact, he synthesized lines from his 2-D LDI sims a few years ago – these are shown in Fig. 24. We could potentially use them here.

Oblate clumps lead to profiles with characteristic shapes that provide poor fits to the data. However, as Oskinova

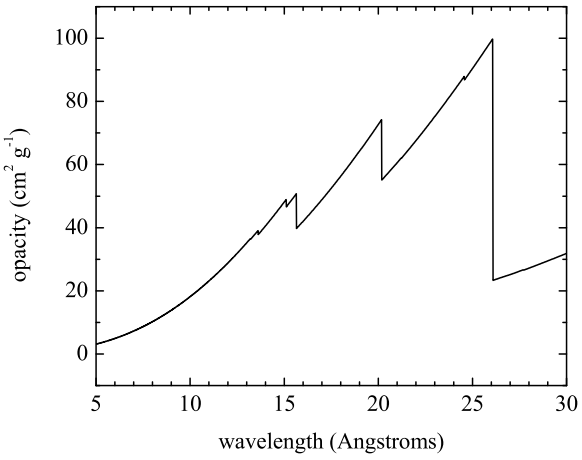

Figure 22. The wavelength dependent opacity of the wind of ζ Pup computed with CMFGEN. Note the prominent K-shell edge of N IV near 26 Å. The unusually large decrement is due to the overabundance of N (3.4 times the solar value from Grevesse & Sauval (1998)) and the underabundance of C, which makes the opacity longward of the N edge lower than it otherwise would be.

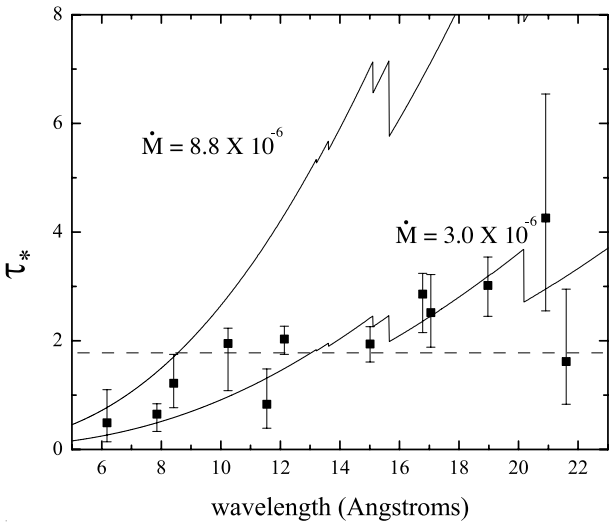

Figure 23. Values of τ_* derived from the non-porous model fits, shown as points with error bars (same as Fig. 13). The value of τ_* expected from the literature mass-loss rate of 8.3×10^{-6} $M_\odot$ yr^{-1} is shown as the upper solid line (*Note to coauthors: after making this figure, we decided to use the more recent value of $\dot{M}$; we haven't changed the figure yet.*). This model has the same wavelength dependence as the opacity shown in Fig. 22. Treating the mass-loss rate as a free parameter, the best fit value of 3.0×10^{-6} $M_\odot$ yr^{-1} is shown as the lower solid line. This model provides a formally good fit. The horizontal dashed line is the best-fit constant τ_* model, as would be expected for a porosity-dominated wind. It does not provide a good fit to the data.

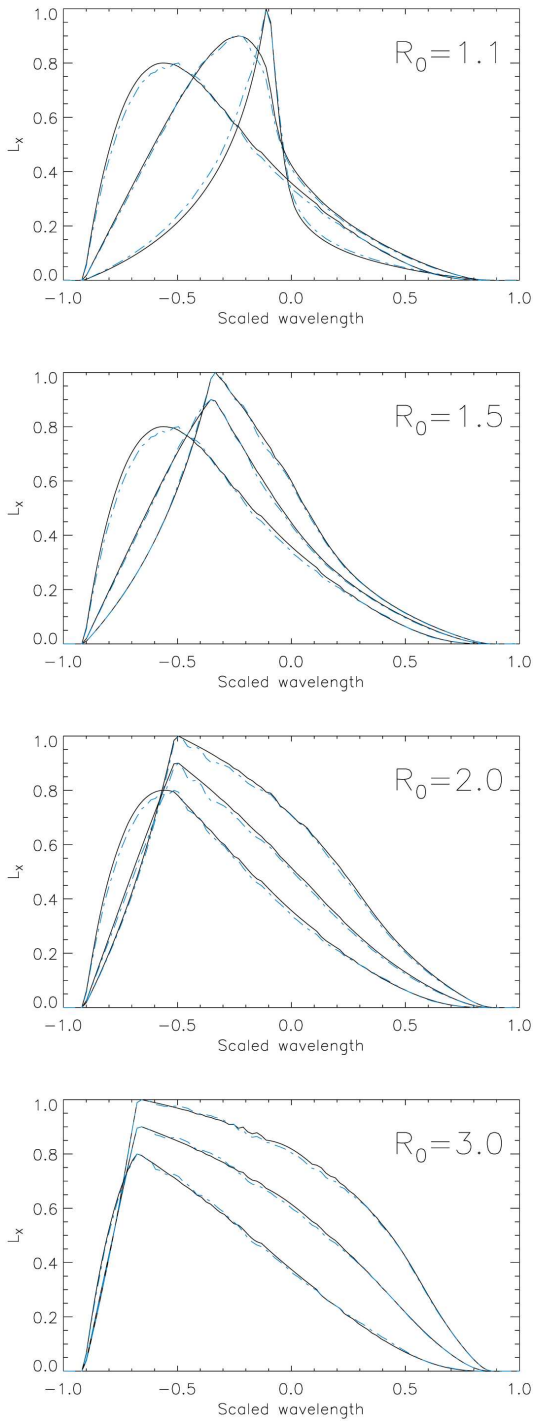

Figure 24. Line profile synthesized from two-dimensional numerical radiation hydrodynamics simulations of the line-driven instability (Dessart & Owocki 2003). The black solid line profiles assume a smooth wind for the radiation transport, while the blue dashed line profiles calculate the radiation transport through the porous wind computed in the simulations. Each frame assumes a different value of R_o, and within each frame, three values of τ_* are plotted ($\tau_* = 1, 2, 5$).

et al. (2006) predicted/implied, oblate clumps do lead to noticeable effects on the X-ray profiles at relatively modest values of the porosity length. It's just that these effects don't make the fits better.

Can we say something about the clump scale and/or spacing by combining the (upper limits to the) porosity lengths along with clumping factors derived from density squared diagnostics?

We have to relate our results to other peoples. This includes OFH's positive contributions; Other people's $\dot{M}$ revisions. And also comment on why Kramer et al. (2003) did not detect the wavelength trend.

7 CONCLUSIONS

ACKNOWLEDGMENTS

We thank...AR7-8002X...

REFERENCES

Berghoefer T. W., Baade D., Schmitt J. H. M. M., Kudritzki R.-P., Hillier D. J., Pauldrach A. W. A., 1996, A&A, 306, 899
Bouret J.-C., Lanz T., Hillier d. J., 2005, A&A, 438, 301
Cash W., 1979, ApJ, 228, 939
Cassinelli J.P., Miller N.A., Waldron W.L., MacFarlane J.J., Cohen D.H., 2001, ApJ, 554, L55
Cohen D.H., Leutenegger M.A., Grizzard K.T., Reed C.L., Kramer R.H., Owocki S.P., 2006, MNRAS, 368, 1905
Dessart L., Owocki S. P., 2003, A&A, 406, L1
Feldmeier A., Oskinova L., Hamann W.-R., 2003, A&A, 403, 217
Feldmeier A., Puls J., Pauldrach A.W.A., 1997, A&A, 322, 878
Fullerton A. W., Massa D. L., Prinja R. K., 2006, ApJ, 637, 1025
Glebocki R., Gnacinski P., Stawikowski A., 2000, Acta Astron., 50, 509
Grevesse N., Sauval A. J., 1998, Sp. Sc. Rev., 85, 161
Hillier D. J., Kudritzki R.–P., Pauldrach A. W. A., Baade D., Cassinelli J. P., Puls J., Schmitt J. H. M. M., 1993, ApJ, 276, 117
Ignace R., 2001, ApJ, 549, 119
Kahn S.M., Leutenegger M.A., Cottam J., Rauw G., Vreux J.–M., den Boggende A.J.F., Mewe R., Güdel M., 2001, A&A, 365, L312
Kramer R. H., Cohen D. H., Owocki S. P., 2003, ApJ, 592, 532
Lamers H. J. G. L. M., Leitherer C., 1993, ApJ, 412, 771
Leutenegger M. A., Paerels F. B. S., Kahn S. M., Cohen D. H., 2006, ApJ, 650, 1096
Leutenegger M. A., Owocki S. P., Paerels F. B. S., Kahn S. M., 2007, ApJ, 659, 642
Lucy L. B., White R. L., 1980, ApJ, 241, 300
MacFarlane J. J., Cassinelli J. P., Welsh B. Y., Vedder P. W., Vallerga J. V., Waldron W. L., 1991, ApJ, 380, 564
Marshall H.L., Dewey D., Ishibashi K., 2004, SPIE, 5165, 457
Oskinova L., Feldmeier A., Hamann W.-R., 2004, A&A, 422, 675
Oskinova L., Feldmeier A., Hamann W.-R., 2006, MNRAS, 372, 313
Owocki S.P., Castor J.I., Rybicki G.B., 1988, ApJ, 335, 914
Owocki S.P., Cohen D.H., 2001, ApJ, 559, 1108
Owocki S.P., Cohen D.H., 2006, ApJ, 648, 565
Perryman M.A.C., et al., 1997, A&A, 323, L49
Press W.H., Flannery B.P., Teukolsky S.A., Vetterling W.T., 2007, Numerical Recipes, 3^{rd} edition. Cambridge, Cambridge University Press
Prinja R. K., Barlow M. J., Howarth I. D., 1990, ApJ, 361, 607
Puls J., Markova N., Scuderi S., Stanghellini C., Taranova O. G., Burnley A. W., Howarth I. D., 2006, A&A, 454, 625
Repolust T., Puls J., Herrero A., 2004, A&A, 415, 349
Runacres M. C., Owocki S.P., 2002, A&A, 381, 1015
van Leeuwen R., 2007a, A&A, 474, 653
van Leeuwen R., 2007b, Hipparcos, the New Reduction of the Raw Data. Springer, Berlin
Vanbeveren D. de Loore C., van Rensbergen V., 1998, A&A Rev., 9, 63